

Robotic Needle Insertion: Effects of Friction and Needle Geometry

M. D. O'Leary¹, C. Simone¹, T. Washio², K. Yoshinaka², and A. M. Okamura¹

¹Department of Mechanical Engineering, The Johns Hopkins University, Baltimore, MD 21218, USA

²Surgical Assist Technology Group, AIST, Tsukuba, Ibaraki, 305-8564 Japan

{marko, aokamura}@jhu.edu, {washio.t, k.yoshinaka}@aist.go.jp

Abstract - Two experiments were performed to determine the effects of friction and needle geometry during robotic needle insertion into soft tissues. In Experiment I, friction forces along the instrument axis were characterized during needle insertion into bovine liver under CT fluoroscopic imaging. Because the relative velocity of the tissue and needle affect viscous and Coulomb friction, the needle insertion process was segmented into several phases of relative motion: none, partial and complete. During the complete relative motion phase, it was found that Coulomb friction accounts for the majority of needle force. In Experiment II, insertion forces along and orthogonal to the needle axis were measured during insertion into a silicone rubber phantom with a consistency similar to liver. The effects of needle diameter and tip type (bevel, cone, and triangle) on insertion force were characterized. A bevel tip causes more needle bending and is more easily affected by tissue density variations. Forces for larger diameter needles are higher due to increased cutting and friction forces. These results may be used in the control of needle insertion for robot-assisted percutaneous therapies.

I. INTRODUCTION

Modeling of the interaction between surgical tools and soft tissue has been the topic of a significant research effort in recent years, e.g. [3,5,7,13]. Such models are necessary for realistic simulation of medical procedures and intelligent autonomous and robot-assisted procedures [4,6].

While there are many types of tools used in medical intervention, we focus this work on percutaneous therapies with needles. Percutaneous therapies are diagnostic or therapy delivery procedures that involve the insertion of tubular delivery devices into targeted locations in the body with the aid of intra-operative imaging devices (e.g. CT, MRI, ultrasound, and fluoroscopy). These delivery apparatuses include instruments such as needles, trocars, bone drills, screws, laser devices, etc. While minimally invasive surgery reduces patient discomfort and decreases recovery time, a major shortcoming is reduced visual and tactile information transmitted to the physician via the instruments. Current clinical methods involve an iterative

manual technique of imaging and positioning, which lacks real-time presentation of information to the operator. In these procedures, it is often the case that sharp surgical instruments, such as needles, come into close proximity to delicate structures that are easily damaged.

The liver was chosen as the initial organ with which to obtain data. The American Cancer Society estimates that 16,600 new cases (11,000 in men and 5,600 in women) of primary liver cancer and intrahepatic bile duct cancer will be diagnosed in the United States during 2002 [1]. Liver biopsy is a percutaneous procedure that is often used to diagnose the cause of chronic liver disease. It is also used to diagnose liver tumors identified by imaging tests. In many cases, biopsy is used to confirm chronic liver disease, as well as determine the amount of damage to the organ. Liver biopsy is also used after liver transplantation to determine the cause of elevated liver tests and determine if rejection is present [2]. One approach to treating liver cancer is via ablation. Ablation refers to methods that destroy the tumor without removing it, and is also a percutaneous procedure.

A. Previous Work

To date, a number of researchers have explored ways to improve surgeons' skills in procedures where little visual and direct tactile feedback exists. These mainly take the form of haptic simulators, for procedures such as catheter insertion [8], lumbar puncture [9], epidural blocks [4,10], endoscopic surgeries [18], and laparoscopic surgeries [14]. While most of the previous work has focused on improving clinical therapies through training, the goal of this research is to develop models that can be used in real-time robotic assistance.

In the areas of telemanipulation and human-robot cooperation, there are a few examples of reality-based modeling used in medical procedures. Yen, et al. [19] describe a telemanipulation system for assisting in the penetration of soft tissue for medical tasks. The system interacts with the environment through a rotating arm that performs needle insertion. They construct a simulation using velocity and acceleration information calculated from encoder readings of a single test of a porcine sample. Brett, et al. [3] presented an automated handheld device to interpret the type and deformation of tissue while being inserted into recently deceased porcine and human lumbar



Fig. 1. Setup for Experiment I: friction experiments under CT Fluoro imaging. The liver is suspended between two clear acrylic plates.

samples. Components measured include syringe pressure, force, and needle displacement. The surgeon controls the instrument's motion. There has also been recent work in the area of specialized surgical devices that can acquire *in vivo* data [5,13]. DiMaio and Salcudean have developed a two-dimensional finite element model and simulation for needle insertion based on experiments with phantom soft tissues [6,7]. This paper builds upon the authors' previous research in needle insertion modeling [11,12,17].

II. EXPERIMENT I: FRICTION FORCES

The purpose of this experiment was to measure friction forces during needle insertion, independent of other force sources such as tissue stiffness and cutting. While the experiment was performed with bovine liver, the methodology could be used with any soft tissue.

A. Experimental Setup

Data was acquired using a 1-degree-of-freedom translation stage to guide a 1.27mm O.D., 15.24 cm long surgical needle into bovine liver. A 1-axis 10N capacity Entran™ load cell was used to measure forces in the direction of motion. The control software executed on a Windows NT Pentium II 450 MHz computer with a graphical user interface that we developed. We recorded time, position of the needle, and force at a frequency of 500 Hz. Data was acquired from five bovine livers. Imaging data was gathered with a clinical Toshiba Multi-Slice Aquilion 0.5 CT Fluoro™ machine. Fig. 1 shows the setup for experiments performed under CT Fluoro imaging.

Since there are several forces acting on the needle, it is important to model each force. These forces can be

described as the stiffness force of the entire organ before puncture occurs, friction force, and the force required to cut through the internal tissue. The friction force occurs along the length of the needle inside the tissue, and is due to tissue adhesion and damping. We used a modified Karnopp friction model as described in [17]. This representation allows for stiction by using a static constant of Coulomb friction that is higher than the dynamic constant.

$$F_{\text{friction}}(\dot{z}, F_a) = \begin{cases} C_n \operatorname{sgn}(\dot{z}) + b_n \dot{z} & \dot{z} \leq -\Delta v \\ \max(D_n, F_a) & -\Delta v < \dot{z} \leq 0 \\ \min(D_p, F_a) & 0 < \dot{z} < \Delta v \\ C_p \operatorname{sgn}(\dot{z}) + b_p \dot{z} & \dot{z} \geq \Delta v \end{cases} \quad (1)$$

where C_n and C_p are the negative and positive values of dynamic friction, b_n and b_p are the negative and positive damping coefficients, D_n and D_p are the negative and positive values of static friction, \dot{z} is the relative velocity between the needle and tissue, Δv is the value below which the velocity is considered to be zero, and F_a is the sum of non-frictional forces applied to the system (which includes inertial effects and force due to elasticity of the tissue during any pre-sliding displacement of the liver). In order to properly identify the friction and damping coefficients, force data was obtained by passing a needle completely through one lobe of a liver whose thickness is known so that there is always a constant amount of tissue in contact with the needle at any time.

A sinusoidal velocity of the needle was chosen to obtain force data at a range of smooth velocities. Repeated periodic motion along the same vertical line prevents cutting of new tissue, resulting in force measurements due to friction and inertia alone. The procedure for these experiments is the same as that described in [17], with the addition of CT Fluoroscopy. Imaging allowed us to identify portions of data with differing relative velocities between the needle and liver.

B. Results

Examination of CT Fluoro images revealed different phases within the force vs. insertion depth profiles. In each direction of motion (insertion or removal), there are three distinct phases of data that correspond to varying relative velocities between the needle and the liver. The demarcation of these phases is dictated by the acrylic plates that constrain the liver motion. Figs. 2 (force data) and 3 (imaging data) show the important positions and three phases of relative motion between the needle and tissue: (a) no relative motion, (b) partial relative motion, and (c) complete relative motion:

Phase (a) occurs from when the needle and liver are at a maximum position and velocity has just started to be non-zero (positions 1 and 5), to when the liver first contacts the plate and the bulk of its mass stops moving because of this constraint (positions 2 and 6).

Phase (b) occurs from the point where the liver first contacts the plate, although there is still some tissue motion at the hole where the needle is allowed to pass (positions 2 and 6), to when the tissue has completely stopped moving and is at its maximum position (positions 4 and 8). This phase can be further segmented into (b1) and (b2). Phase (b1) occurs from the time at which the liver first contacts a plate (positions 2 and 6) to when the liver fully contacts the plate (positions 3 and 7). Phase (b2) occurs from the time at which the liver fully contacts a plate (positions 3 and 7), although there is still some tissue motion through the hole, to when the tissue has completely stopped moving and is at its maximum position (positions 4 and 8).

Phase (c) occurs from when the tissue has completely stopped at its maximum position (positions 4 and 8), to when the needle is at its maximum position (positions 5 and 9).

The needle had a constant velocity of 4 mm/s. In phase (a), static friction dominates the behavior of the system, so the liver and needle move in unison. In this case, the velocity of the needle equals that of the liver, so the relative velocity is zero. During phase (b), the portion of the liver not constrained by the plate (at the hole where

the needle passes through the plate) is still in motion. In this case, the velocity of the liver is smaller than that of the needle, which results in some relative velocity between them. In phase (c), the tissue is no longer moving, resulting in a relative velocity equaling that of only the needle, so that phase (c) is completely dominated by the dynamic friction. For the purposes of modeling,

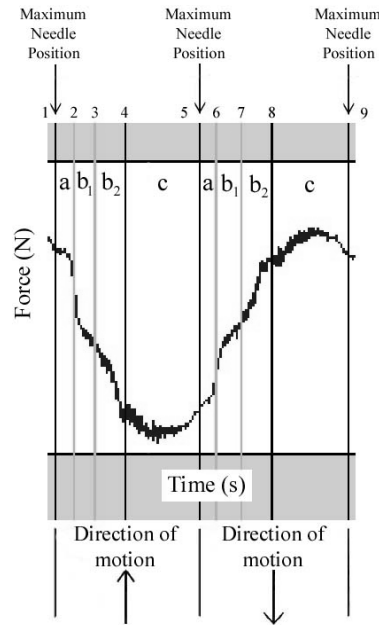


Fig. 2. Needle insertion phases, demarcated by relative velocity of needle and tissue.

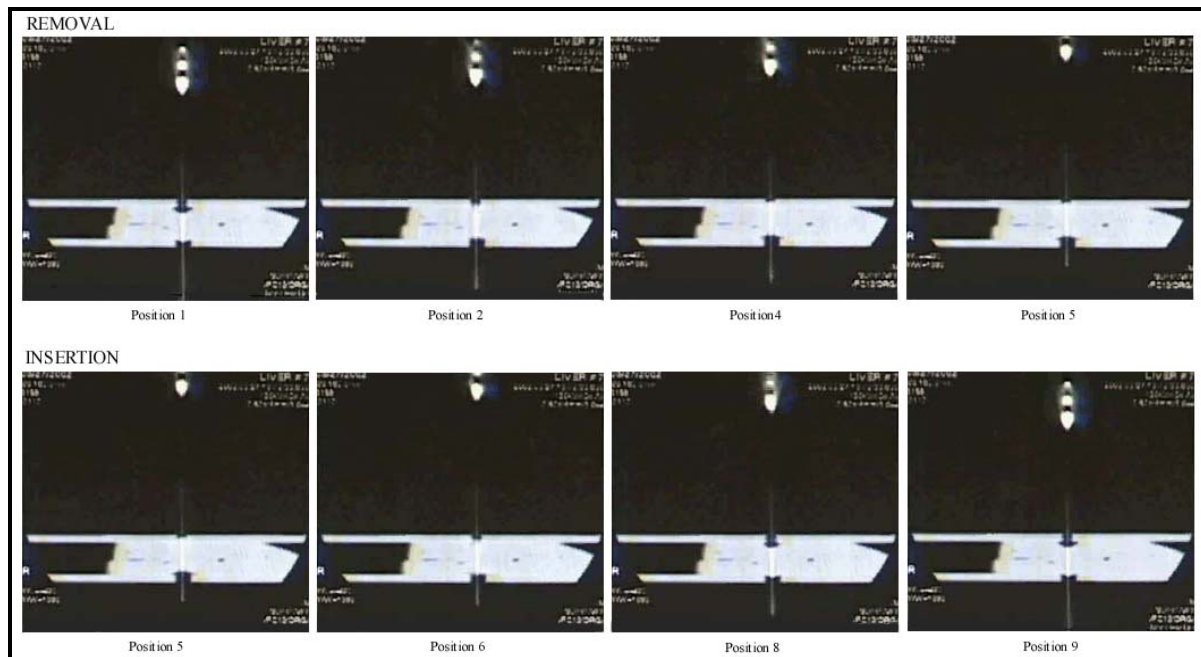


Fig. 3. CT Flouro images acquired during a periodic needle insertion into a liver.

Table 1. Friction parameter values for bovine liver.

Parameter	Mean	Standard Deviation
C_p (N/m)	10.57	4.34
C_n (N/m)	-11.96	4.40
b_p (N-s/m ²)	212.31	45.70
b_n (N-s/m ²)	-293.08	30.73
D_p (N/m)	18.45	5.42
D_n (N/m)	-18.23	4.30

only the data with known relative velocity are used to compute the coefficients of static and dynamic friction.

The data was analyzed using a Matlab™ program, adapted from [15]. The data input includes time, position, mass and force of the needle. The data must be segmented to model the two types of friction, static and dynamic. To obtain the coefficients of static friction, data corresponding to phase (a) was used. To determine the coefficients of dynamic friction and damping coefficients, data corresponding to phase (c) was used. The velocity was assumed to be zero around a band of 0.005 mm/s (determined by the boundary of phase (a)), so data in that interval was removed from the dynamic friction analysis. The remaining data was separated according to positive and negative velocities. The parameters measured for a 0.2 Hz sinusoidal insertion are shown in Table 1. The same liver was tested at 10 different points, generating large standard deviations due to variation in tissue properties at different locations in the liver.

C. Imaging Limitations

A problem with using CT Fluoro imaging lies in the way that it forms final images. The Toshiba Aquilion CT Fluoro™ machine acquires four simultaneous 0.5 mm slices in every 0.5-second rotation of the gantry. These four slices are converted into three simultaneous images on the display. One image represents the slice just before the target, one is the slice right after the target, and one image combines two slices for a high-resolution view of the target. Because the diameter of the needle is small, it is usually only visible in the combined center image. Thus, when imaging is complete, the needle is difficult to see. Another limitation is that in general, it is not sensitive enough to pick up fine tissue details, only some major blood vessels in the viewing field. This is because the contrast of the view must be adjusted to minimize the presence of artifacts from the metal in the slice. However, it is sufficient because the tissue and needle motion are easily viewed, and is the best imaging technology available for these types of experiments. X-ray imaging requires implanted fiducials, which change the mechanical properties of the tissue.

III. EXPERIMENT II: EFFECTS OF TIP TYPE AND NEEDLE DIAMETER

The purpose of this experiment was to characterize the effect of needle diameter and geometry on insertion forces. Silicone rubber phantoms were used in order to test needle effects without the complications resulting from the inhomogeneous internal structure of real tissues.

From the data, we are able to draw several correlations between needle diameter, tip type, axial force, and orthogonal force (needle bending). However, due to the lack of tissue deformation data, a complete characteristic equation of the forces cannot be constructed. The reader is referred to [7] for a 2-D characterization of needle insertion that includes tissue deformation, although needle geometry effects are not analyzed.

A. Experimental Setup

A cylindrical sample of silicone rubber (100mm diameter, 40mm height) was used as the phantom tissue. The exact material properties of the phantom are not relevant to this analysis. Stainless steel needles of various diameters and tip types were fixed to a 6-axis force sensor. Table 2 lists the tip types, tip angles, and diameters of the needles used in the experiment. The sensor has a maximum load capacity of 20N for the x and y (orthogonal) directions and 50N for the z (axial) direction. Voltage data from the force sensor was recorded via National Instruments LabVIEW™ software at a rate of 250 Hz in the x , y , and z directions. (No torque data was recorded.) Calibration data was used to determine the corresponding forces. The data was smoothed using a running mean with a 100 point window. To track the position and shape of the needle, a bi-planar X-Ray system developed at AIST was used. Images were recorded at 30 frames per second and appeared as shown in Fig. 4.

The needles were inserted into the rubber at a constant velocity of 2.65mm/s for 7 seconds. The needle then remained in the rubber for 5 seconds and was

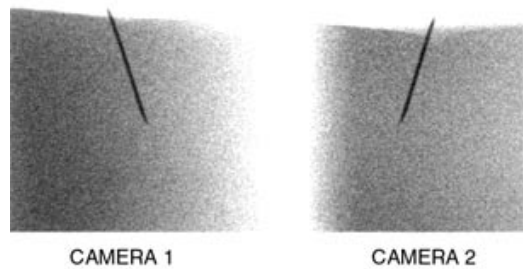


Fig. 4. Images taken from bi-planar X-Ray at 7 seconds into insertion.

Table 2. Diameters and cut angles of needles used in experiment.

Bevel Tip	Cone Tip	Triangular Tip
0.65mm - 14°	0.59mm - 28°	0.59mm - 49°
0.75mm - 14°	0.95mm - 28°	0.95mm - 49°
1.00mm - 10°	1.55mm - 28°	1.55mm - 49°
1.00mm - 14°		
1.00mm - 20°		
1.35mm - 14°		
1.55mm - 14°		

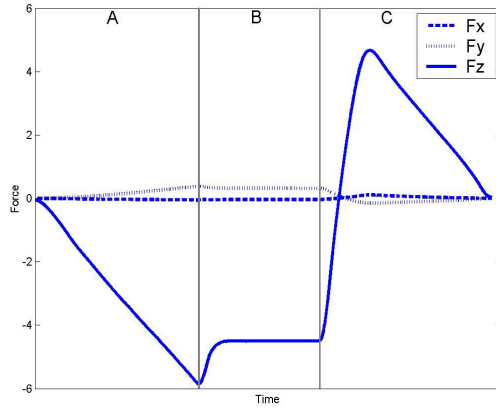


Fig. 5. Force versus insertion depth for a 1.00mm, 14° bevel needle, during insertion (A), holding (B), and extraction (C).

subsequently extracted. This procedure was repeated three times for each of the needles in Table 2. Between each trial, the rubber sample was relocated to create an unpunctured sample for each needle insertion.

B. Results

Clear phases of insertion, relaxation, and extraction can be seen in the smoothed force data. In Fig. 5, section A shows the insertion of a 1.00mm bevel-tip needle. Section B shows the 5-second interval where the needle is motionless. Here, the force on the needle relaxes logarithmically. Section C shows the forces due to extraction. Although one cannot extract useful information from sections B and C without tissue deformation data, section A reveals two effects of needle geometry, which are described in the following sections.

B.1 Effect of Geometry on Axial Forces

With the exception of the 0.65mm bevel-tip needle, all of the trials revealed a linear relationship between position and axial force as the needle is inserted. The 0.65mm needle can be fit by second-order polynomial curve; this is

Table 3. Needle type in relation to the average slope of axial insertion forces.

Needle Type	Diameter	Average Slope	Standard Deviation
14° bevel	0.75	-0.263	0.010
10° bevel	1.00	-0.308	0.009
14° bevel	1.00	-0.309	0.011
20° bevel	1.00	-0.320	0.015
14° bevel	1.35	-0.420	0.017
14° bevel	1.55	-0.469	0.033
28° cone	0.59	-0.276	0.006
28° cone	0.95	-0.328	0.015
28° cone	1.55	-0.552	0.005
49° TP	0.59	-0.171	0.006
49° TP	0.95	-0.251	0.002
49° TP	1.55	-0.360	0.007

most likely caused by a large amount of needle bending (discussed in the next section).

When a line is fit to the insertion section of the data (section A), the resulting slopes show an expected trend (Table 3). As the needle diameter increases, the more the rubber is displaced and compressed in the vicinity of the needle. This increases the forces normal to the surface of the needle, leading to higher friction forces.

As shown in Table 3, the force vs. position slope increases as the needle diameter increases for each of the tip types. To verify the accuracy of this and other relationships, t-tests were performed on the data samples with alternative hypothesis $\mu_x > \mu_y$, where μ_x and μ_y are the means of the two sample sets compared. Table 4 shows the p-values for various relationships. When testing if a larger needle diameter has a significantly larger force slope, all of the p-values are acceptable within a 95% confidence interval. Referring to Table 3, the 1.00mm needle causes slightly larger slopes as the degree of the bevel tip increases. This change in slope can be explained not from friction, but from the change in the amount of the needle face that is exposed to the axial direction. However, no correlations can be drawn at this time between axial forces and bevel angle since the p-values between these needles are not within the acceptable range.

When comparing different tip types, Table 4 shows triangular pyramid (TP) tips as having the least resistance forces, then bevel, then cone. Two sizes of needles were tested between tip-type groups—medium and large (small was not considered because a first-order polynomial could not be appropriately fitted to the 0.65mm bevel data). The only exception to tip-type ordering was when comparing the medium bevel tip and medium cone tip. This p-value did not fall within the accepted range, implying that there

Table 4. P-values for various two-sample t-test with an alternative hypothesis of $\mu_x > \mu_y$.

x-sample	y-sample	p-val
0.75mm bevel	1.00mm bevel 14°	0.003
1.00mm bevel 14°	1.35mm bevel	0.000
1.35mm bevel	1.55mm bevel	0.043
0.59mm cone	0.95mm cone	0.002
0.95mm cone	1.55mm cone	0.000
0.59mm TP	0.95mm TP	0.000
0.95mm TP	1.55mm TP	0.000
Medium TP (.95)	Medium Bevel (1.0)	0.000
Large TP	Large Bevel	0.002
Medium Bevel	Medium Cone (.95)	0.072
Large Bevel	Large Cone	0.006
10° Bevel	14° Bevel	0.469
14° Bevel	20° Bevel	0.176

is a threshold of needle diameter where the cone and bevel tip needles begin to behave similarly.

B.2 Effect of Geometry on Needle Bending

Upon insertion, noticeable amounts of force orthogonal to the needle axis were observed, implying significant bending of the needle. This bending was verified by the X-Ray images. The standard equation for deflection of a cantilever beam is dependant on the second moment of area and thus the needle diameter. Therefore, the bending forces ($f_x^2 + f_y^2)^{0.5}$) should decrease as the needle diameter increases. In actuality, the bending forces increase with needle diameter. This is due to the fact that forces are higher overall for larger needles. To get a true relationship between needle diameter and bending, a ratio of maximum bending force to maximum axial force was used (the maximum force being at the instance of zero velocity). The results of this relationship for different tip types can be seen in Fig. 6.

Fig. 6 clearly shows how the bending forces tend to decrease as the needle diameter increases. However, it also shows that beveled needles bend much more than cone or TP tipped needles. This is due to the fact that a bevel tip is not symmetric and receives higher forces on one side, which causes bending. This raises the question of why the cone and TP tip bend if they are symmetrical.

From our data, it appears that the two symmetrical needles bend because small, random density inconsistencies in the silicone rubber. Since it is virtually impossible to determine the locations of these inconsistencies, the bending that occurs is somewhat random. The fact that the data points for the beveled needle in Fig. 6 are not as consistent as those for the other two needles shows that the beveled needle is more susceptible to changes in the material.

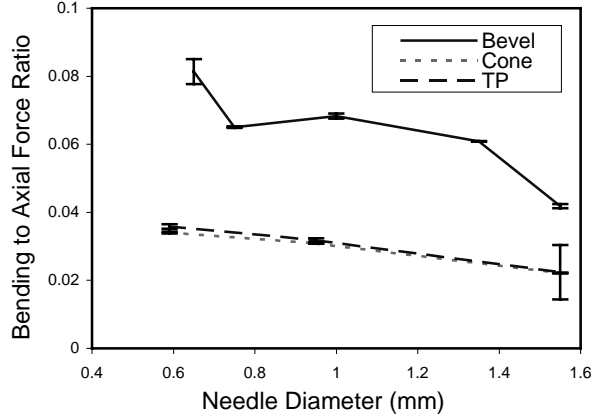


Fig. 6. Bending Ratio versus Needle Diameter for three tip types with error bars.

C. Discussion

From the results presented above, it is clear that size and shape of the needle play an important role in determining the forces of needle insertion. In short, smaller needle diameters lead to less resistance force but more needle bending. Bevel tipped needles also lead to more bending where as cone and triangular pyramid tips have less and somewhat more consistent bending. It can also be seen that the TP tips have less resistance force than bevel and cone tips, and that cone tips cause the highest resistance forces.

IV. CONCLUSIONS AND FUTURE WORK

This paper presents methodologies for the measurement of friction forces and needle geometry effects during the insertion of needles into soft tissues. The friction models developed and knowledge of geometry effects can be used in the design of virtual environments for simulation of percutaneous therapies, and the planning and execution of robot-assisted procedures.

A complete model of the forces arising during needle insertion into soft tissues will require a combination of empirical and analytical modeling. It is likely that the most inclusive models will result from a combination of finite-element deformation modeling approaches (such as in [7]) and specialized experiments to extract particular force sources (such as those presented in this work). Future work in this field should include more thorough testing, the development of new testing and modeling methodologies, and multiple model (e.g. deformation and friction) integration. More needles sizes and tip types should be tested, including those currently used for percutaneous procedures. Future experiments will include

the use of phantom tissues of varying material properties embedded with fiducials and/or appropriate sensors. In addition, the models developed will be used to guide robot-assisted diagnosis and therapy.

V. ACKNOWLEDGEMENTS

This material is based on work supported by the United States National Science Foundation (grants EEC9731478 and EEC0121940), Japan National Institute of Advanced Industrial Science & Technology, and a Vredenburg Fellowship from the Johns Hopkins University. We thank Yanagisawa Shinichi for assistance in the setup and execution of experiments.

VI. REFERENCES

- [1] American Cancer Society, "What Are The Key Statistics for Liver Cancer?" <http://www.cancer.org/>.
- [2] American Liver Foundation, "Liver Biopsy," <http://www.liverfoundation.org/>.
- [3] P. N. Brett, A. J. Harrison, and T. A. Thomas, "Schemes for the Identification of Tissue Types and Boundaries at the Tool Point for Surgical Needles," *IEEE Transactions on Information Technology in Biomedicine*, Vol. 4, No. 1, 2000, pp. 30-36.
- [4] P.N. Brett, "Simulation of resistance forces acting on surgical needles," *Proceedings of the Institution of Mechanical Engineers*, Part H, Vol. 211 (H4), 1997, pp. 335-347.
- [5] I. Brouwer, *et al.*, "Measuring In Vivo Animal Soft Tissue Properties for Haptic Modeling in Surgical Simulation," *Medicine Meets Virtual Reality* 2001, pp. 69-74.
- [6] S. P DiMaio and S. E. Salcudean, "Simulated Interactive Needle Insertion," *Proceedings of the 10th Symposium on Haptic Interfaces for Virtual Environment and Teleoperator Systems*, 2002, pp. 344-351.
- [7] S. P. DiMaio and S. E. Salcudean, "Needle insertion modelling and simulation" *Proceedings of the IEEE International Conference on Robotics and Automation*, 2002, pp. 2098-2105.
- [8] E. Gobbetti, *et al.*, "Catheter Insertion Simulation with Co-registered Direct Volume Rendering and Haptic Feedback," *Medicine Meets Virtual Reality*, 2000, pp. 96-98.
- [9] P. Gorman, *et al.*, "A Prototype Haptic Lumbar Puncture Simulator," *Proceedings of Medicine Meets Virtual Reality*, 2000, pp. 106-109.
- [10] L. Hiemenz, *et al.* "A Physiologically Valid Simulator for Training Residents to Perform an Epidural Block," *Proceedings of the IEEE Biomedical Engineering Conference*, 1996, pp. 170-173.
- [11] H. Kataoka, T. Washio, M. Audette, and K. Mizuhara, "A Model for Relations between Needle Deflection, Force, and Thickness on Needle Penetration," *Proceedings of the Fourth International Conference on Medical Imaging and Computer-Assisted Intervention*, 2001, pp. 966-974.
- [12] H. Kataoka, T. Washio, K. Chinzei, K. Mizuhara, C. Simone, and A. Okamura, "Measurement of Tip and Friction Force Acting on a Needle During Penetration," *Proceedings of the Fifth International Conference on Medical Image Computing and Computer Assisted Intervention*, 2002, pp. 216-223.
- [13] M. P. Ottensmeyer and J. K. Salisbury, "In Vivo Data Acquisition Instrument for Solid Organ Mechanical Property Measurement," *Proceedings of the Fourth International Conference on Medical Image Computing and Computer-Assisted Intervention*, 2001, pp. 975-982.
- [14] S. Payandeh, "Force Propagation Models in Laparoscopic Tools and Trainers," *Proceedings of the IEEE Engineering in Medicine & Biology International Conference*, 1997, pp. 957-960.
- [15] C. Richard, M. R. Cutkosky, and K. MacLean, "Friction Identification for Haptic Display," *Proceedings of the American Society of Mechanical Engineers, Dynamic Systems and Control Division*, Vol. 67, pp. 327-334.
- [16] C. Simone, "Modeling of Needle Insertion Forces for Percutaneous Therapies," M. S. Thesis, Department of Mechanical Engineering, The Johns Hopkins University, May 2002.
- [17] C. Simone and A. M. Okamura, "Haptic Modeling of Needle Insertion for Robot-Assisted Percutaneous Therapy," *Proceedings of the IEEE International Conference on Robotics and Automation*, 2002, pp. 2085-2091.
- [18] V. Vuskovic, *et al.*, "Realistic Force Feedback for Virtual Reality Based Diagnostic Surgery Simulators," *Proceedings of the IEEE International Conference on Robotics and Automation*, 2000, pp. 1592-1598.
- [19] P. Yen, R. D. Hibberd and B. L. Davies, "A Telemanipulator System as an Assistant and Training Tool for Penetrating Soft Tissue," *Mechatronics*, Vol. 6, No. 4, 1996, pp. 423-436.